Scalable-resolution structured illumination microscopy

ANKIT BUTOLA,[1,2,*] **SEBASTIAN ACUNA,**[1,2] **DANIEL HENRY HANSEN,**[1] **AND KRISHNA AGARWAL**[1]

[1]*Department of Physics and Technology, UiT The Arctic University of Norway, Norway*
[2]*Co-first authors*
ankitbutola321@gmail.com

Abstract: Structured illumination microscopy suffers from the need of sophisticated instrumentation and precise calibration. This makes structured illumination microscopes costly and skill-dependent. We present a novel approach to realize super-resolution structured illumination microscopy using an alignment non-critical illumination system and a reconstruction algorithm that does not need illumination information. The optical system is designed to encode higher order frequency components of the specimen by projecting PSF-modulated binary patterns for illuminating the sample plane, which do not have clean Fourier peaks conventionally used in structured illumination microscopy. These patterns fold high frequency content of sample into the measurements in an obfuscated manner, which are de-obfuscated using multiple signal classification algorithm. This algorithm eliminates the need of clean peaks in illumination and the knowledge of illumination patterns, which makes instrumentation simple and flexible for use with a variety of microscope objective lenses. We present a variety of experimental results on beads and cell samples to demonstrate resolution enhancement by a factor of 2.6 to 3.4 times, which is better than the enhancement supported by the conventional linear structure illumination microscopy where the same objective lens is used for structured illumination as well as collection of light. We show that the same system can be used in SIM configuration with different collection objective lenses without any careful re-calibration or realignment, thereby supporting a range of resolutions with the same system.

1. Introduction

The past few decades have witnessed widespread application of fluorescence microscopy in biology by providing the unique ability of intrinsic selectivity, chemical specificity and signal to background ratio. In the recent times, technical advancement in fluorescence microscopy are primarily focused on simultaneous imaging of different cellular/sub-cellular components, three dimensional imaging of thick samples such as organoids, and improving spatial resolution of imaging [1–3]. In particular, several methods have been proposed in the past to break the classical resolution limit. These methods can be broadly categorized into the following groups: a) stimulated emission and depletion (STED) [4,5], b) single molecule localization (SML) i.e., rely on the fact localization precision [6–9], c) intensity fluctuations based optical nanoscopy (IFON) [10–14], and d) structured illumination microscopy (SIM) [15–18]. STED, SML and IFON all rely on photokinetics of fluorophores, i.e. the variation in the photon emission statistics either naturally (IFON), or using long-lived dark states (IFON, SLM), or trigger of different photophysical behaviour in presence of specific laser lights of high intensity (STED, SML). Consequently, strict control, special dyes and/or special imaging protocols are needed for these techniques. This restricts versatility of the methods. Furthermore, the temporal throughput of SML and IFON is quite low due to the need of adjusting the acquisition rate and the number of frames to the photokinetics. Temporal throughput of STED is limited due to point scanning based illumination and acquisition. These restrictions are absent in SIM, making it more versatile

and preferred in wide scenarios, despite lower factor of resolution enhancement than the other techniques.

Super resolved imaging in SIM is achieved by illuminating the sample by structured patterns and computationally combining the high frequency information conventionally in the Fourier space. Structured illumination extends the diffraction limit by an amount equal to the spatial frequency of the illumination pattern. Since the highest spatial frequency of the illumination pattern is diffraction limited, the best enhancement of lateral resolution in SIM is by a factor of about two [19]. Two-factor resolution enhancement is valid in the case of linear SIM i.e., when emission intensity is proportional to the excitation wavelength. Non-linear SIM can provide further resolution enhancement [18–20], but it uses extremely high intensity to saturate the excited state of molecules, which results in non-linear relation between the emission rate per fluorophore and the illumination intensity.

Another limitation of the conventional SIM-based system is the use of same objective lens for creating structured illumination and also for collecting the light from the sample. If one intends to support SIM with another objective lens of a different numerical aperture, recalibration and realignment of the system become imperative. This not only increases the demand on cost, but mandates complicated procedure during the process of imaging. The central reason for this limitation is that precise knowledge of the illumination patterns, including the pattern shift and rotation, is crucial for the reconstruction algorithm of SIM.

Our goal is to circumvent the limitation of fixed resolution of SIM system and the requirement of precise knowledge of illumination patterns to achieve super-resolution in SIM. We also intend to reduce the sensitivity of SIM reconstruction to the signal to background ratio. It has been reported that SIM reconstruction algorithms pose certain stringent requirements on the signal quality [21]. As explained in section 2, we achieve our goals by using (a) using non-saturated high frequency illumination pattern achieved within linear optical regime and (b) reconstructing the image using non-linear reconstruction algorithm that does not require illumination to be known a priori. We show in-principle support for resolution enhancement better than the linear structured illumination by decoupling the illumination and detection path and using high NA objective lens for illumination. Experimental results with multiple collection objective lens are shown for validation and wider applicability of the proposed system. We show good reconstructions at signal to background ratio as small as <3.

The motivation of using different collection objective lenses also comes from the potential applications. The dimensions of structures inside cells vary greatly. For example, cytoskeleton on its largest scale of visualization and function spans the entire cell (10s of μm) and requires visualization of <200 nm at its smallest scale. In addition, upgrading the system with switchable laser source and use the best super-resolution for actin and microtubules (<200 nm), the next to best for mitochondria (0.5- 3 μm), and the subsequent one for the cell membrane of cytoskeleton scale. Further, operating in linear regime without the knowledge of illumination simplifies the optical system design and implied relatively inexpensive, easy-to-use instrumentation. We show that the same system can achieve scalable resolution by using the same illumination objective lens, but employing different collection objective lenses. As a consequence, our framework opens up a new possibility for structured illumination based super-resolution techniques.

2. Principle and deviation from the conventional SIM

The essence of SIM lies in being able to introduce precisely known clean high frequency peaks in the illumination pattern in order to (a) down-modulate the high frequency components of the specimens into the collection optical transfer function (OTF) in a systematic manner, and (b) design a simple reconstruction algorithm that solves a linear system of equations derived from the prior knowledge of the illumination pattern. In order to circumvent the need of structured

illumination to achieve super-resolution, both the conditions above have to be relaxed by removing the need of precise peaks corresponding to sinusoidal patterns.

The present article proposes a unique solution to the above problem. We develop a simplified structured illumination system by decoupling illumination and detection arm and employ a reconstruction approach that does not assume sinusoidal illumination patterns. The fundamental empowering component of our approach is to deviate from the conventional SIM and NL-SIM in terms of not needing clean peaks corresponding to sinusoidal illumination patterns.

Our solution comprises of two complementary components shown in Fig. 1(a,b):

- **Easy to align instrumentation with structured illumination pattern:** We present a simple and efficient optical system working in linear regime to induce structured illumination and thereby down-modulate the high frequency components of the specimens into the imaging objective lens's OTF. The presented framework may employ, in principle, random digital patterns or encoded patterns (such as Hadamard, etc.) with translations and rotations regardless of the final resolution desirable, making our method more robust and flexible. For simplicity, we use binary periodic patterns of sufficiently high frequency and project them onto the sample through an illumination objective lens (see Fig. 1(a) and Supplementary Fig. S1). Consequently, the higher frequency components of the binary patterns are blurred by the OTF of the illumination objective lens at the sample plane. The blurred patterns therefore do not have clean peaks corresponding to higher frequency components of the binary pattern needed for conventional SIM reconstruction (see Fig. 1(c)). Nonetheless, problems associated with high illumination intensity are avoided.
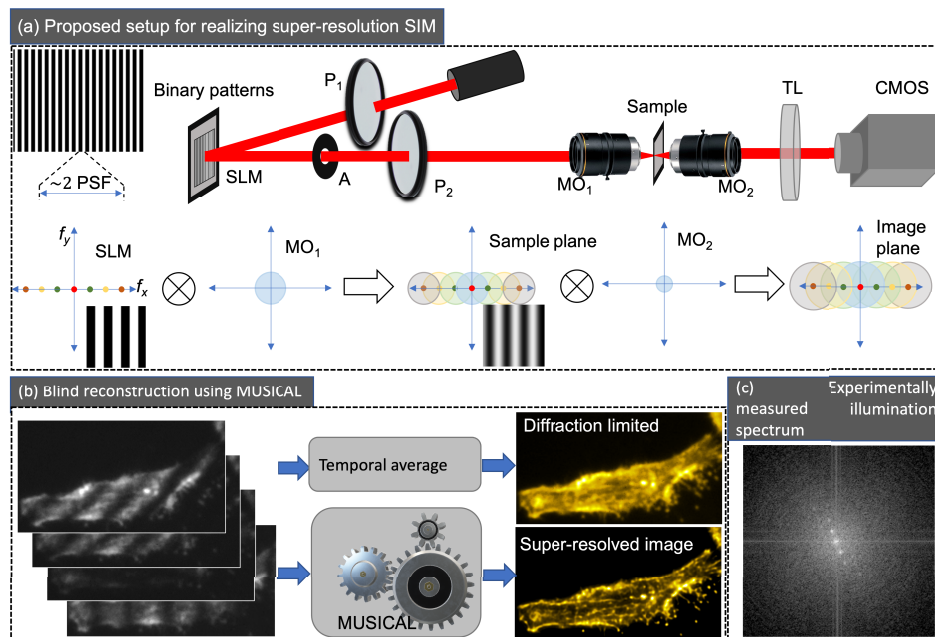

Fig. 1. Overview of proposed imaging an reconstruction technique. (a) Binary patterns are projected into the sample using spatial light modulator to encode high spatial frequency components. (b) Raw datasets with different illumination orientation processed using Multiple signal classification algorithm (MUSICAL). (c) experimentally measured higher order frequencies using binary pattern

- **Illumination blind reconstruction algorithm:** A non-linear reconstruction algorithm is used which does not require the prior knowledge of illumination patterns, nor needs to estimate the illuminations as an intermediary step. For this purpose, we use the principle of pseudospectral decomposition which isolates the spatial frequency components of the illuminated samples that can be well separated from noise for reconstruction. This alleviates the need of knowing or estimating individual illumination patterns. For simplicity of adaptation, we use multiple signal classification algorithm (MUSICAL [14]), which is based on pseudospectral decomposition and has been adapted as a reconstruction approach recently [22] (see Fig. 1(b)). We note that other blind reconstruction algorithms may be employed, and special illumination priors may be incorporated for example when using Hadamard or other computationally exploitable patterns.

3. Methods

3.1. Experimental setup

The experimental setup and illumination strategy is shown in Fig. 1. A collimated laser light beam passes through a polarizer (P_1). The polarized light is modulated using spatial light modulator (SLM), which has a binary pattern supporting high spatial frequencies. This pattern is projected on to the sample through the cross polarizer and illumination objective lens MO_1. Therefore, the pattern on the sample is the clean frequency peaks of the original digital pattern convolved with $MO'_1 s$ OTF. The sample is placed in a plane somewhere between the 'f' and '2f' planes of the illumination objective lens MO_1. The blurring due to MO_1 and the imperfect projection of the pattern implies that only a few peaks that fall within the bandwidth of MO_1 reach the sample. However, this does not pose a problem because we do not need to know or estimate the illumination pattern in our reconstruction.

The design of the illumination pattern is discussed in section 3.2. The sample, labeled with fluorescent dyes, emits photons in response to these illuminations. These photons are collected by imaging optics through imaging microscope objective MO_2 and matching tube lens (TL) on an image sensor array. In order to fully automate the data acquisition and synchronize the SLM pattern projection and camera acquisition, we designed an image acquisition code in labVIEW. We used Cobolt laser of wavelength 660 nm, SLM Pluto-2.1 from Holoeye, 60X, 0.9NA (RMS60X-PFC, Olympus) objective lens for MO_1, different options for MO_2, tube lens matching the MO_2, and ORCA-Fusion C14440-20UP sCMOS camera for the image sensor array. In addition, polarization control is maintained by two polarizers in the illumination path and SLM.

Our motivation to use SLM for illumination modulation was two-fold. First, SLM is an electronic device which implies illumination patterns can be changed without mechnical movements. Second, the pixel size of the SLM was 8 μm, which together with the MO_1 and MO_2 gives sufficient sampling of the point spread function (PSF) of the MO_2. However, we note that other digital adaptive optical devices (such as digital micromirrors) or analog binary phase or amplitude masks could have been used instead of SLM without the loss of generality.

Further, we used MO_1 and MO_2 to be two distinct microscope objective lenses in transmission setup in order to investigate the effect of the illumination objective lens independent of the collection, and use different combinations for the objective lens for understanding the advantage accrued by the high spatial frequencies of illumination.

3.2. Selection of illumination patterns

The selection of the illumination patterns, in our case, is treated as a geometric and signal processing problem.

Periodicity Given the numerical aperture (NA) of MO_2, twice the null-to-null width (w) of the PSF is used as the period of the binary pattern. The duty cycle of the binary pattern is 50%. The choice of 3× or 1× the width of the PSF results in deteriorated results. The reason is explained through an illustration in Fig. 2(a). Consider an Airy point spread function with null-to-null width w. Convolving a binary pattern of periodicity $2w$ results in the best modulation depth together with minimum flat components of maximum and zero intensity. Having larger flat components implies less level of fluctuations in two consecutive pattern shifted images. The advantage of using larger period is also manifest in better robustness to noise, this is illustrated in Supplementary Fig. S2. Indeed, one could use smaller period (say only of size (w)), which results in half the number of images per orientation, and therefore better temporal resolution. However, the tradeoff is threefold: (a) poorer modulation depth, therefore (b) lesser fluctuations, and (c) poorer robustness to noise. More numerical experiments with different periodicities are presented in Supplementary Note S1 and Supplementary Fig. S4.
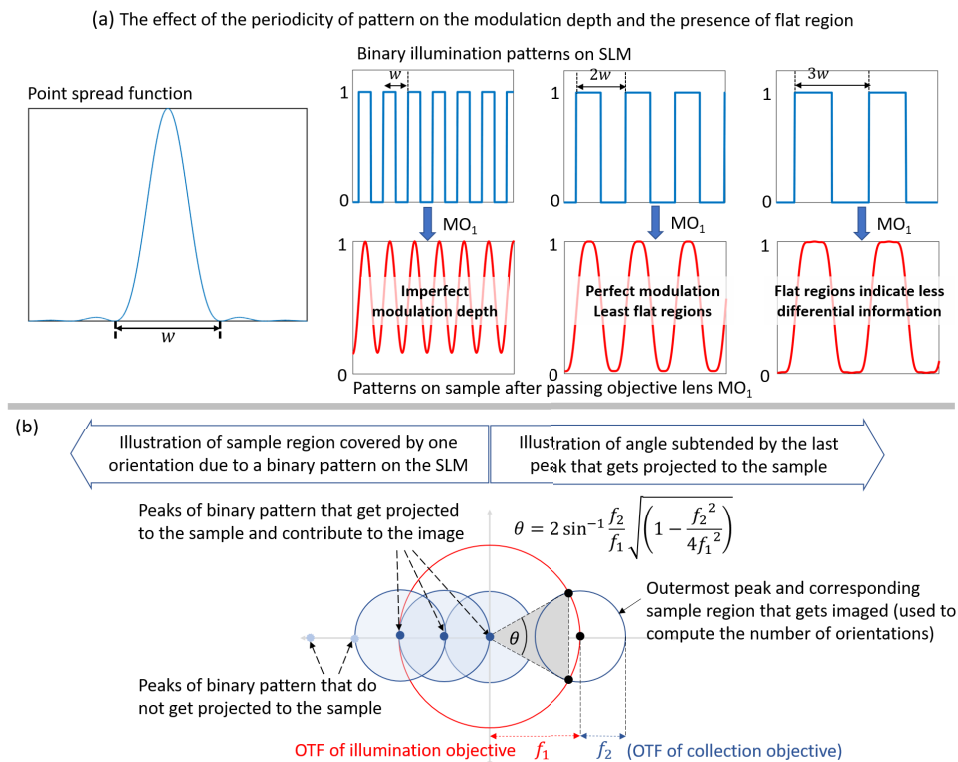

Fig. 2. The selection of parameters of the binary pattern projected on MO_1 before illuminating the sample. (a) Selecting periodicity other than ~ $2w$ leads to either poor modulation depth or flat regions of maximum or no illumination, both of which reduce differential information between two consecutive translated illumination patterns. (b) The illumination and collection objective lenses determine what region in Fourier space of the sample gets images and how many orientations are needed for for imaging the sample without having shadow regions in the Fourier domain. (c) For a more general scenario, the scheme in (b) presents some limitations.

Pattern shifts (i.e. translations) In order to have uniform illumination for a given orientation, we introduce shifts in patterns by one pixel of SLM at a time for the entire period of the binary pattern. Uniformity of illumination can be achieved in principle using just two patterns, namely a binary pattern and its Boolean inverse, However, shifting one pixel at a time allows for introducing

the maximum diversity of spatial fluctuations at every point in sample. Further study on the pattern shift is presented in Supplementary Note S2 and Supplementary Fig. S4.

Orientations Given the desired order of resolution enhancement K over FWHM ($\sim w/2$) and the effective size of OTF (proportional to $1/(2w)$) of MO_2, we compute the number of orientations such that there is no shadow region within the desired bandwidth. This is illustrated in Fig. 2(b). It is simply specified using the smallest integer exceeding π/θ, where $\theta = \sin^{-1}(2/K)$. However, this assumes that period $2w$ was used. Attempting to incorporate a more general scenario, such as with a different selection of period of patterns and/or f_1 including the effect of noise presents challenges. We therefore include a more sophisticated scheme of coverage of desired spectrum in Supplementary Note S3 and Supplementary Fig. S5. We note that the analyses discussed here pertain to the minimum number of orientations needed. We present a discussion regarding using more orientations than necessary in Supplementary Fig. S6 and Supplementary Note S4.

The parameters derived from the above considerations Given the 660 nm laser light and the MO_2 i.e., 10X (0.25 NA, RMS10X Olympus), 20X (0.4 NA, RMS20X Olympus) and 40X (0.65 NA, RMS40X Olympus) the null-to-null width $w \approx \lambda/NA$ is ~ 2640, ~ 1650 and ~ 1015 nm respectively. Further, the pixel size of SLM (8 μm) combined with 60X of MO_1 illumination implies that the w in SLM pixels is approximately 20, 13 and 8 pixels. Thereby the periodicity of the patterns is 40, 26 and 16 pixels, the number of pattern shifts is 40, 26 and 16 per orientation. Further, we used 90 orientations, where two consecutive orientations differed by 2°. This covered the entire 360° since each orientation is symmetric along the origin. The oversampling in the orientation is intentional so that the best achieved resolution is limited only by noise in the images. Further, we optimized the number of pattern required to achieve super-resolution imaging for different objective lens in the Supplementary Table S1.

3.3. Blind reconstruction approach for super-resolution

We use MUSICAL for blind reconstruction of the sample. While MUSICAL was originally envisioned for widefield illumination, its capabilities allows its use also for structured illumination microscopy. This was proved already in [22] where MUSICAL was used with images where the sample was illuminated using a lattice projecting structured illumination on it. A nice feature of the algorithm is that every illumination is inherently used without a precise knowledge of it. The key feature of illumination patterns exploited in MUSICAL is that fluctuations at the same point in the sample region occur in different time frames from the variety of illumination patterns. This implies that no illumination estimation algorithm is needed as a pre-processing or tandem processing step. As a consequence, not only the entire computation is rather simple, also the sensitivity of the reconstruction to errors in illumination estimation is not a concern.

MUSICAL's algorithm The algorithm is a combination of Singular Value Decomposition (SVD) and the knowledge of the PSF of the system together with the mathematically linear model of imaging discussed in the supplementary document of the original article [14]. Let's consider a sequence of images taken for a particular sample stained with fluorescent molecules. The intensity emitted by these molecules is a random variable and they can be considered as independent sources or emitters. If this sample is imaged in time, we can obtain a sequence of images which we then call an image stack. If every image in the stack is flattened to be represented as a column vector, then the entire stack, can be expressed as single rectangular matrix I whose columns correspond to each single frame in the stack. This allows its decomposition using SVD as I = USV with U and V being square matrices and S a diagonal matrix. Due to the structure of I, we can conclude that the information of its columns is encoded in U. Further, S contains in its diagonal the singular values of the matrix associated to the respective columns of U. We refer to these as the eigenvalues and the eigenimages of the stack. Then, the columns of U, or eigenimages, form a basis of the image stack originally acquired. Among others properties, these vectors are orthogonal and ordered by their statistical importance in

terms of how much information they contain with respect to the particular sample. On the other hand, the stack can be modeled as a convolution of the original emitters distribution $E(\mathbf{r})$ and the point-spread-function of the optical $G(\mathbf{r})$, where both terms are considered as scalar functions and $\mathbf{r}$ is a two-dimensional vector containing the coordinates in the imaging plane. Then $I(\mathbf{r}) = G(\mathbf{r}) * E(\mathbf{r})$ with $*$ meaning convolution. Additionally, if the sample is formed by K different emitters, then its underlying structure can be expressed as a discrete sum of K impulses centered in the location of the emitters. This is $E(\mathbf{r}) = \sum_{k=1}^{K} b_k \delta(\mathbf{r} - \mathbf{r}_k)$. We can then use the properties of the impulse function and express the image as $I(\mathbf{r}) = \sum_{k=1}^{K} b_k G(\mathbf{r} - \mathbf{r}_k)$. Here, b_k is the intensity of each individual emitter. Furthermore, in the discrete case this can be more easily expressed as the matrix multiplication $\mathbf{I} = \mathbf{G}\mathbf{E}$ where we have use bold letters to indicate column vectors. In this expression, $\mathbf{I}$ corresponds to a single image whose values correspond to the intensity measured at different sensor or pixels. G is the matrix of K columns containing the point-spread-function of the system but shifted at the location of the different emitters. Finally, $\mathbf{E}$ correspond to the values of b_k. If b_k were to vary in time, then we can acquire a stack as defined previously. In this case, the stack can also be expressed as a matrix multiplication as I = GE. From this, it is possible to conclude that the columns of G span the entire space of images regardless of the values of E which can be considered as random. If the same stack were to be decomposed using SVD as explained before, then the space spanned by G would be the same than the one spanned by U. If the number of pixels is P, then U has P columns. The assumption in MUSICAL is that the rank, or the number of non-zero eigenvalues, of I is less than P. If the rank is S, then it means that the image can be formed only from the span of the S first eigenimages. This is called the signal subspace. On the other hand, the remaining eigenimages are considered as forming the noise subspace. Due to the orthogonality of U, both spaces are orthogonal. However, images are affected by noise and in turn, real images are full-ranked which makes separation non-trivial. In order to deal with this problem, MUSICAL separates the space using the eigenvalues and a threshold given by the user. The eigenimages with eigenvalues above such threshold are considered as the signal, and the one below, noise.

After such separation is made, we can exploit the fact that the signal space spanned by the eigenimages is the same than the space spanned by the columns of G. As a consequence, the columns of G are orthogonal to the noise space and therefore its projection on the noise space is zero. Based on the projections this can be used to define an indicator function which allows to test an arbitrary point by comparing the point-spread-function centered at that point, and the eigenimages obtained from the actual image. The indicator function is expressed below in Eq. (1).

$$f(\mathbf{r_t}) = \left(\sqrt{\frac{\sum_{i \in Signal} |\mathbf{u_i} \cdot \mathbf{g_t}|^2}{\sum_{i \in Noise} |\mathbf{u_i} \cdot \mathbf{g_t}|^2}} \right)^{\alpha} \tag{1}$$

Here, $\mathbf{u}_i$ corresponds to the columns of U indexed by the index i, and $\mathbf{g_t}$ is the image of a single test emitter indexed by t given by the shifted PSF of the system. The indicator function assigns a numerical value at points in the sample, where this numerical value indicates the presence of fluorophore. In practice, these points are located on a grid finer than the one given by original pixels, reducing the pixel size of the resulting image when compared to the original image. The factor α is a contrast enhancement factor whose value is based on heuristics.

In terms of processing, MUSICAL is carried out using a moving window that process a small patch at the time, instead of the entire field of view. The patch corresponds to a section of the size of the main lobe of the point-spread-function in the lateral coordinates, but including all the temporal information. These patches overlap and their corresponding super-resolved images are then merged by averaging in order to obtain a MUSICAL image of the entire field of view. The total number of patches correspond to the total number of pixels in the lateral plane.

A final note on the indicator function is presented here. This can be modified to combine signal and noise using a weighting function [23]. This is called soft MUSICAL or MUSICAL-S and allows leave the threshold out of the indicator function. The weighting is a function of the eigenvalues and allows to include partially information of noise into the numerator of the indicator function, and signal into the denominator.

Illumination patterns and MUSICAL In the conventional form of MUSICAL, the fluctuations in fluorescence emissions from emitters occurs as the temporal information encoded in V and the spatial distribution of the emitters gets encoded in the signal space of U. However, in the application presented here, each frame corresponds to a different illumination pattern. Therefore, the variation of illumination intensities at pixels over time is encoded in V and the ensemble of spatial distributions of the illumination patterns is encoded in the signal space of U together with the sample distribution. The mathematical derivations related to the form in which the illumination patterns are encoded in U were presented in the supplementary information of [24] and [22]. The relevant portions of the derivations are reproduced in our Supplementary Note S5. Here, the derivations of [22] directly apply and thereby the maximum possible resolution supported by MUSICAL (in the case of best selection of algorithmic parameters) is given by $2(k_{\max} + k_{\mathrm{MO}_2})$, where $k_{\max}$ is the maximum frequency supported by the illumination patterns and k_{MO_2} is the maximum frequency supported by the collective objective lens. It is however worth noting in our case that $k_{\max}$ depends upon the noise present in the image as the noise levels determine the farthest peak in the illumination spectrum that is separable from the noise floor.

As described previously, U contains structural information in its columns or eigenimages. And since the number of matrices U is generally large, studying them is challenging. In the following section we explain how we have carried out a small analysis of the eigenimages of these matrices to show how they differ in therms of the information they carry.

The analysis is done by creating images using a single eigenimage from each patch. The selection criteria is based on the order that every eigenimage has in its own matrix U. So, an image of the eigenimage of order i is build using the following function:

$$f(\mathbf{r_t})^{(i)} = |\mathbf{u_i} \cdot \mathbf{g_t}| \tag{2}$$

As can be seen Eq. (2), the expression corresponds to the projection of the PSF on a determined eigenimage. The stitching procedure is the same than for MUSICAL as describe previously with the patch-based processing. In Fig. 3 we show a visual example of the relation between U using the projection of eigenimages of different orders, the diffracted-limited image, and the MUSICAL result. The first row show the actual images that were obtained using this method, in addition to the diffracted-limited and MUSICAL image. To improve visualization, these were normalized following different procedures. For the diffracted-limited and super-resolved they were first normalized by its maximum value as $I_N(\mathbf{r}) = I(\mathbf{r})/\max_{\mathbf{r}}(I\mathbf{r})$. For the projections of eigenimages, the normalization involves the set of all of them. Let o be the order of an eigenimage. The, the normalization is carried as $I_N^{(o)}(\mathbf{r}) = I^{(o)}(\mathbf{r})/\max_{\mathbf{r},o} I^{(o)}(\mathbf{r})$. This allows a fairer comparison between different orders in terms of intensities value in the images. The images are presented in logarithmic scale of base 10. The bottom row shows the Fourier Transform of the corresponding image shown in top. These were normalized as $I_N(\mathbf{r}) = |I(\mathbf{r})/\max_{\mathbf{r}}(I(\mathbf{r}))|^2$ and then plotted in logarithmic scale as well. Looking to the first to columns, the first we observe is how MUSICAL provides a richer frequency content thanks to its super-resolution properties. Second, we notice how the projection of the first eigenimage (Fig. 3(c),top) do not contain information for super-resolution as can be see in the smaller radius in the frequency domain (Fig. 3(c),bottom) when compared to the diffracted limit. This reduction is due to the stitching process as technically the first eigenimage corresponds actually to the diffracted-limited image when only a single patch is considered. More interesting is that the projection of higher orders (Fig. 3(e),top) provide in fact more frequency content than the diffraction-limited but not more

than MUSICAL as the latter combines all the information available in the eigenimages. Finally, it's interesting to note that even though the signal decreases and the background increases as we move to higher orders, the spectrum seems invariable in terms of coverage. We observed that the coverage in the frequency domain seems the same except for the first order. However, a study of this phenomena goes beyond the scope of this manuscript.
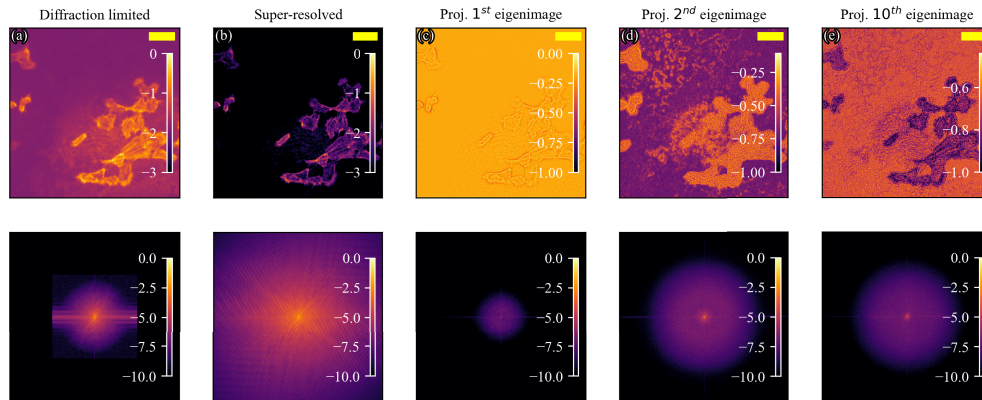

Fig. 3. The Fourier Transform allows to compare the spectrum of the diffracted image and the MUSICAL result in sample of Actin acquired with a 10x, 0.25 NA objective. Scale bar is 50 μm. The upper row displays different images after a logarithmic transformation in base 10, while the bottom shows their corresponding Fourier Transform.

3.4. Sample preparation, data acquisition and data processing

We consider 2 types of samples in our experiments, namely bead samples with known bead diameters and actin in HeLa cells. The sample preparation, data acquisition, and data processing details for the different samples are presented here. A customized mount system is designed to hold and image the sample.

Bead sample The sample was prepared in the cover slip. Tetra beads of diameter 200 nm (Tetraspeck, Thermofisher T7279) were employed and excitation/emission wavelength of 660/690 nm were used for them. The stock solution of tetra beads was diluted in proportion 1:50 in distilled water. 100 μL of the solution was added on the petri dish and allowed to dry completely. We used 40X, 0.65 NA objective lens for MO_2. The exposure time of acquisition is 200 ms per frame.

HeLa cells sample HeLa cells were grown in Dulbecco's Modified Eagle Medium (DMEM) supplemented with 10% fetal bovine serum and 1% penicillin/streptomycin in a standard humidified incubator at 37°C with 5% CO_2. Cells were seeded into the glass bottom petri dish 1−2 days before imaging. For imaging, the cells were washed in PBS and fixed in 4% paraformaldehyde for 15 minutes. Cells were then washed with PBS and permeabilized with 0.1% Triton X-100 in PBS for 4 minutes, and washed three times in PBS. Cells were then incubated with Atto-647N phalloidin in PBS for 20 minutes in order to label F-actin in the cells.

These samples were imaged using different objective lenses for MO_2 in order to assess the resolution scalability with the same illumination strategy but using different collection optics. These samples were also used to perform several supplementary studies. In the results reported in the main article, we used four candidate objective lenses for MO_2, namely 10X (0.25 NA), 20X (0.40 NA), 40X (0.65 NA) and 50X (0.55 NA). The exposure time in either case is 100 ms per frame.

3.5. Data acquisition and analysis

Total 1260 illumination patterns were used to generate super-resolution images in case of beads and Hela cells. However, number of patterns were further optimized to achieve super-resolution with minimum frames. All the raw datasets were processed using MUSICAL, without any preprocessing. Soft-MUSICAL version reported in [23], which alleviates the need of user-specified threshold. Python implementation of the algorithm was used. Further, we used $\alpha = 4$ (refer to Eq. (1) above) and sub-pixelation of 10 i.e., one pixel in the raw image corresponds to 10×10 pixels in the MUSICAL generated image. Raw and processed images presented in the article have been pseudocolored using standard colormaps available on imageJ platform. The selection of the colormap and the intensity range is done heuristically for good visualization, as conventional for microscopy data visualization.

3.6. Resolution estimation

In order to estimate the resolution enhancement, we used decorrelation analysis to estimate the resolution of the computationally generated super-resolved images [25]. It has been shown in the past to overcome the limitations of Fourier ring correlation [25]. While performing the decorrelation analysis, we used the Matlab implementation provided by the authors, and set the parameter for sampling the frequency domain as 50 and the number of low-pass filters as 30. In order to convert the cut-off frequency k_c given by the tool into resolution in metric system, we used the formula given by the authors, $r = \frac{2*p}{k_c}$, where p is the pixel size.

4. Results

Results on 200 nm beads We first demonstrate the resolution improvement of the present approach by imaging 200 nm fluorescent beads. The collection objective lens is 40X (0.65 NA) and the illumination objective is 60X (0.9 NA), which corresponds to diffraction limit of ~445 nm. Therefore the beads are smaller than the expected resolution enhancement of linear SIM. Further, some of these beads are spaced within the classical diffraction limit, also closer than the resolution achievable by linear SIM as well.

Average of the images taken using our illumination patterns is shown in Fig. 4 (left and middle panels) as a representative of diffraction limited image. The middle panel shows two region of interests (ROI), each with cluster of beads placed relatively densely. These images are reconstructed using MUSICAL to utilize non-linear patterns introduced in the acquired datasets. The results are shown in the right panel of Fig. 4 for the chosen ROIs.

In order to quantify the resolution enhancement achieved by our method, we measured the PSF from the image of few single beads across the sample in the diffraction limited (average of all images) and the super-resolved images. The average full width at half maximum (FWHM) of the single beads is 946 nm. On the other hand, the average FWHM of the same beads in the super-resolved image is ~ 347 nm, roughly 3× the diffraction limit.

In addition to FWHM, we also estimated resolution using decorrelation analysis. The resolution observed in diffraction-limited image is 954 nm and in super-resolved 376 nm. Therefore, the resolution enhancement is found approximately 2.54. This agrees with the qualitative results as well, as we explain here. A crop from diffraction-limited image that appears qualitatively similar to two crops from super-resolved image are identified in Fig. 4. Each of these crops appear to have two beads placed close to each other. The line profiles across the two beads are also plotted for each crop. It is seen from the line profiles that the beads in the diffraction-limited crop are separated by ~ 1069 nm, while for the super-resolved crops are 400 nm and 368 nm respectively. This indicates also a resolution enhancement by ~ 2.6 to 2.9 times. The resolutions obtained by decorrelation analysis are plotted as a function of number of orientations in Supplementary Fig. S2.
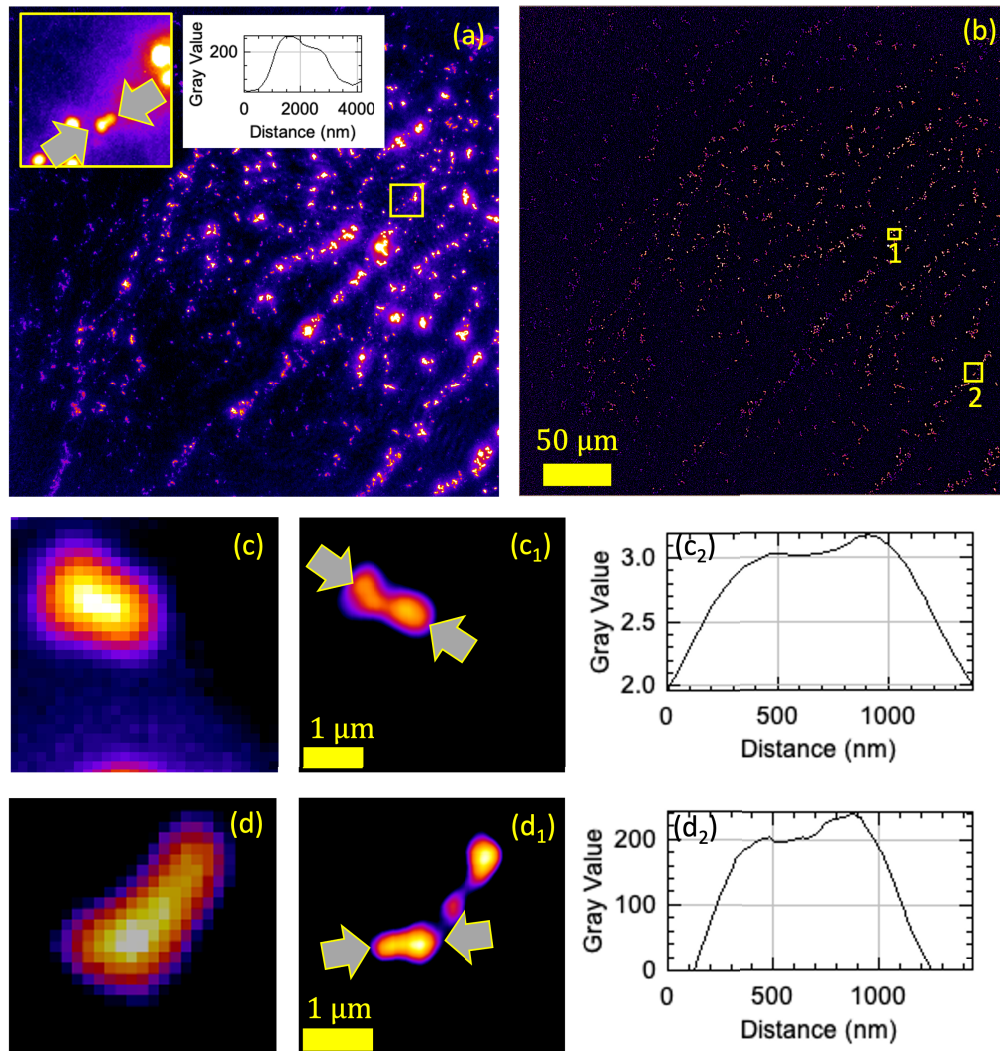
Fig. 4. Resolution improvement beyond the diffraction limit, shown using sample containing 200 nm beads. 40X,0.65 NA objective lens is used for collection of light. Diffraction limit is ~445 nm, resolution observed in diffraction limited image is 954 nm and in super-resolved 376 nm. Region a shown as an inset in top-left panel is diffraction limited and visually similar to the super-resolved versions of regions 1 and 2 shown in top-right panel and zoomed-in in the lower panels.

Actin filaments in cells Fig. 5 presents the results for actin filaments. It shows the comparison of diffraction limited image and our super-resolved reconstruction of actin filaments of Hela cell using two different objective lenses. Figure 5(a) depicts the superposition of average images and super-resolved images of the the sample using 10X, 0.25 NA. The same ROI is imaged by 50X, 0.55 NA lens and shown in Fig. 5(b). The zoom-ins of one region of interest, shown using white rounded rectangle in Fig. 5(a), are shown for the 10X diffraction limited, 10X super-resolved, 50X diffraction limited, and 50X super-resolved images in Fig.5 (c1-c4), respectively. Analogously, the zoom-ins of another ROI, shown using sharp cornered rectangle in Fig. 5(a), are shown in Fig. 5(d1-d4). The results show improvement of contrast and sharpness using our approach in
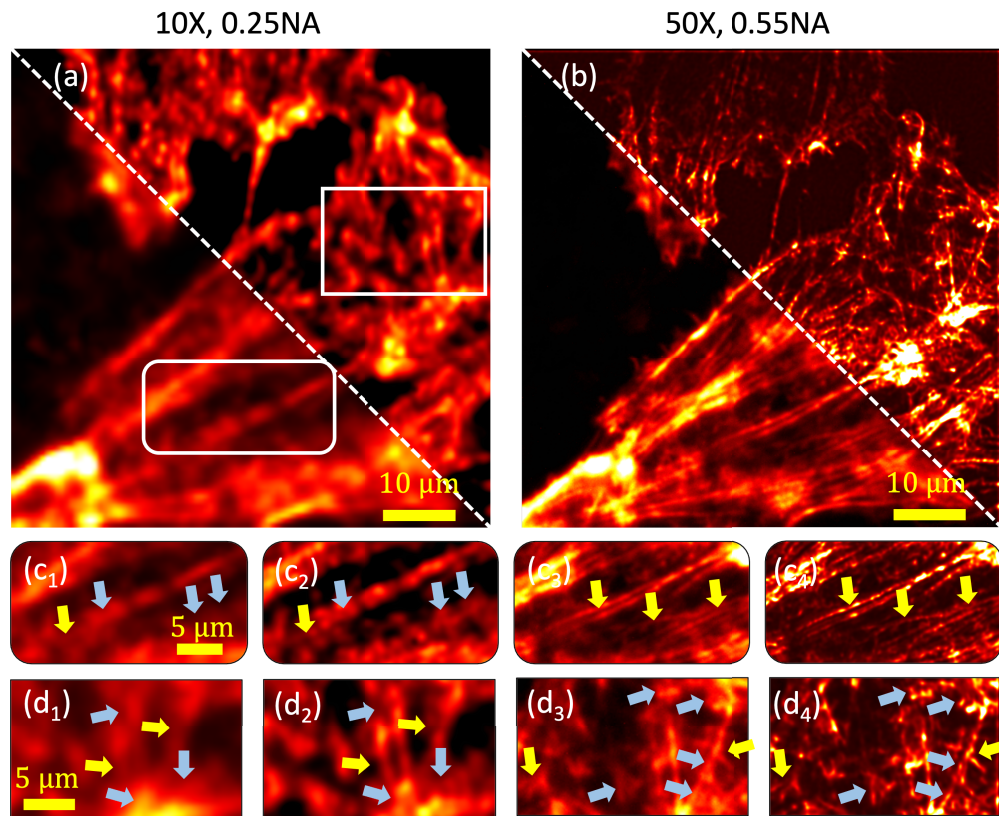
Fig. 5. Super-resolution imaging of actin filaments in Hela cells. a) Image acquired with a 10X, 0.25NA lens and a super-resolved image. b) Similar field of view is imaged by 50X, 0.55 NA lens. Smaller ROI are magnified and shown in c1-c4 and d1-d4). Yellow arrows point at contrast enhancements leading to better visualization. Cyan arrows show resolution enhancement leading to better feature details.

sparse regions (shown using yellow arrows), and enhancement of resolution in the dense regions (shown using cyan arrows) of the diffraction limited image. The regions which are not resolved in 0.25 NA (Fig. 5(c1, d1)) are marked and compared with the super-resolved image (Fig. 5(c2, d2)) generated from the datasets acquired using 0.25NA. Figure 5(c2, d2) can also be compared with the Fig. 5 image of 0.55 NA (Fig. 4(c3, d3)). It is seen that the features in Fig.5(c2, d2) generally match well with Fig. 5(c3, d3), with some mismatch of finer details. The possible reason could be the sample preparation, mechanical instability in the system and polarization sensitivity of the SLM. Since SLM is an polarization sensitive device, contrast of the illuminated pattern could be directional dependent. Nonetheless, the issue could be overcome simply by replacing the sample mounting stage with the fine rotational stage and synchronize with the illumination pattern.

The decorrelation analysis for the data acquired using 10X indicated a resolution of 1856 nm in the diffraction limited image and 480 nm for the super-resolved image. This indicates a resolution enhancement of approximately 3.77 times. The decorrelation analysis for the data acquired using 50X indicated a resolution of 697 nm for the diffraction-limited image and 254 nm for the super-resolved. This indicates a resolution enhancement of approximately 2.74. The resolution measured in the diffraction limited and super-resolved images for both collection objective lenses are presented in Supplementary Fig. S2. Furthermore, we have shown the application of current work only using low NA detection since. Since, high NA lenses have limited working distance,
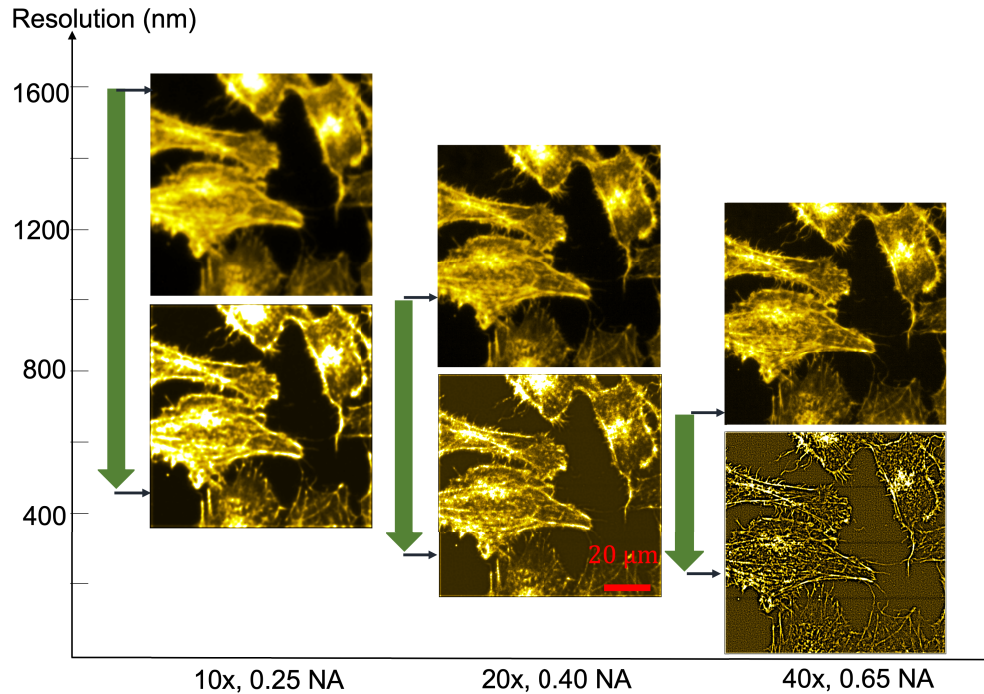
Fig. 6. Pattern optimization for super-resolution imaging with different collection lenses. Similar region of interests is imaged by three different NA (0.25, 0.40 and 0.65) without any re-calibration. Scale bar: 20 μm.

more precise alignment of the system will be required to achieve super-resolution on higher NA lenses. Further accommodation for using liquid immersion medium is a consideration if a special sample holder is designed for the purpose. On the other hand, low NA lens capture images with larger depth of field and larger field-of-view, which is desired in many applications.

Multiscale resolution Finally, we optimized minimum number of pattern and angles required to achieve super-resolution images using different collection lenses. We used three different collection objective lens i.e., 10X (0.25NA), 20X (0.45 NA) and 40X (0.65 NA) and acquired the datasets of actin filaments of the Hela cells. Period of the binary pattern is selected twice the null-to-null width of the PSF of collection lens. Details of the optimum number of angles is simulated and presented in Supplementary Fig. S5 and Supplementary Fig. S7 and Table S1. Simulated protocols is verified experimentally where 20° rotation angle is found suitable for 10X, 0.25 NA to fill OTF symmetrically. On the other hand, 60° is well suited for 20X, 0.45 NA and 40X, 0.65 NA lens. Therefore, total number of frames required to achieve super-resolution images in case of 10X, 20X and 40X are 360, 78 and 48 respectively. The diffraction limited and super-resolved images for each case is shown in Fig. 6. Experimentally observed resolution and the resolution enhancement for each collection geometry is shown in Table 1. Note that, increasing numerical aperture of the collection objective lens decreases the number of photons per pixel therefore the signal to background strength decreased in high NA objective lens. Experimentally calculated resolution in case of 0.25 NA, 0.40 NA and 0.65 NA is found to be 1718 nm, 987 nm and 681 nm respectively. The results show resolution enhancement by a factor of 1.96, 3.40 and 2.68 for 0.25 NA, 0.40 NA and 0.65 NA, respectively. Even though the signal to background ratio for 0.40 NA and 0.65 NA is 3.03 and 2.40, which is considered inadequate in case of conventional SIM, our approach offers resolution enhancement by a factor of 3.40 and 2.68. In Supplementary notes S6 and Supplementary Fig. S8 and S9, we have compared fluctuation based technique

such as MUSICAL, SOFI, SRRF and open source SIM reconstruction tool i.e., FairSIM in low signal to background SIM data. We addressed the artifacts of the methods under two different levels of signal to background ratio (SBR). The sample can be imaged with high SBR in SIM and low SBR in our system to still achieve comparable resolution enhancement. Therefore, the proposed approach could be considered as a simple solution to avoid the instrumentation and computational complexity of SIM. In addition, the entire framework can be applied to different imaging modalities by improving their resolution and field of view.

Table 1. Experimental diffraction limited resolution and super-resolution using different collection objective lens. Factor of resolution enhancement of 2-3.5 with signal to background ratio of 2.4-5.9. Note that signal to background ratio of 2.4-5.9 considered inappropriate in conventional SIM reconstruction approach. Less resolution enhancement in case of 0.25NA is observed because of poor sampling of PSF.

Collection lens (NA_{coll})	Expt. diffraction limited resolution (nm)	Expt. super resolved (nm)	Resolution enhancement	Signal to background
0.25	1718	877	1.96	5.93
0.40	987	289	3.40	3.03
0.65	681	254	2.68	2.40

5. Conclusion

In this work, we have presented a structured illumination approach using linear optical system together with non-linear reconstruction algorithm to achieve super-resolution imaging. Our technique enables more than the conventional 2-fold resolution enhancement of linear SIM. The key enabling idea is to obviate the need of strictly clean peaks in the Fourier spectrum of the illumination by using illumination-blind super-resolution algorithm. The idea is realized through an experimental scheme which introduces an illumination pattern containing high orders of frequency peaks obfuscated by an illumination objective lens that projects binary periodic illumination patterns on the sample. We validate the resolution enhancement using beads sample and actin filaments in cell sample. We show the resolution enhancement using a variety of collection objective lenses, ranging from 10X, 0.25 NA to 50X, 0.55 NA. We used the same illumination objective lens while using the different collection objective lenses, indicating easy scalability of resolution and field-of-view. We use a fixed high NA lens for illumination in the present work therefore the field of view will be limited by the illumination objective lens. The main motivation for this choice was to demonstrate the technique's strength of being able to use different collection lenses. Nonetheless, low NA illumination objective lens can be used to improve the space-bandwidth product of the current approach if desired at almost no extra complication and with a resolution enhancement of only 2x. This can be achieved by replacing the excitation objective lens with a multi-objective lens turret such as used in the collection path.

In addition, the results consistently show resolution enhancement by a factor of 2.6 to 4 because of using high NA condenser lens for the excitation and low NA as a collection objective lens. On the other hand, non-linearity of the reconstruction algorithm supports better resilience to noise as well as better contrast enhancement, which further helps in achieving the said resolution enhancement in very low signal conditions. In the future, we would like to improve the signal strength while balancing the exposure time, light dose, system stability and photobleaching, thereby optimizing the system for living cells with resolution enhancement by a factor of more than 4. We believe that the proposed experimental+computational framework using linear optical system will find wide applicability to many biological applications where simple optical design and super-resolution is essential.

Author contribution

KA conceived the idea and supervised the work. AB designed experimental system and planned the experiments. DHH and AB optimized and automate the system. SA optimized the computational part and reconstructed all the images. AB, SA and KA analysed the result and prepared the figure. AB and KA mainly wrote the manuscript and all author contributed revised the manuscript.

Disclosures. Authors declare no competing interest.

Data availability. Data may be obtained from the authors upon reasonable request.

Supplemental document. See Supplement 1 for supporting content.

References

1. J. W. Lichtman and J.-A. Conchello, "Fluorescence microscopy," Nat. Methods **2**(12), 910–919 (2005).
2. J. F. Dekkers, M. Alieva, L. M. Wellens, H. C. Ariese, P. R. Jamieson, A. M. Vonk, G. D. Amatngalim, H. Hu, K. C. Oost, H. J. Snippert, J. M. Beekman, E. J. Wehrens, J. E. Visvader, H. Clevers, and A. C. Rios, "High-resolution 3D imaging of fixed and cleared organoids," Nat. Protoc. **14**(6), 1756–1771 (2019).
3. G. Devitt, K. Howard, A. Mudher, and S. Mahajan, "Raman spectroscopy: an emerging tool in neurodegenerative disease research and diagnosis," ACS Chem. Neurosci. **9**(3), 404–420 (2018).
4. S. W. Hell and J. Wichmann, "Breaking the diffraction resolution limit by stimulated emission: stimulated-emission-depletion fluorescence microscopy," Opt. Lett. **19**(11), 780–782 (1994).
5. H. Blom and J. Widengren, "Stimulated emission depletion microscopy," Chem. Rev. **117**(11), 7377–7427 (2017).
6. W. Moerner, "Microscopy beyond the diffraction limit using actively controlled single molecules," J. Microsc. **246**(3), 213–220 (2012).
7. J. Schnitzbauer, M. T. Strauss, T. Schlichthaerle, F. Schueder, and R. Jungmann, "Super-resolution microscopy with DNA-PAINT," Nat. Protoc. **12**(6), 1198–1228 (2017).
8. E. Nehme, L. E. Weiss, T. Michaeli, and Y. Shechtman, "Deep-STORM: super-resolution single-molecule microscopy by deep learning," Optica **5**(4), 458–464 (2018).
9. A. Butola, D. A. Coucheron, K. Szafranska, A. Ahmad, H. Mao, J.-C. Tinguely, P. McCourt, P. Senthilkumaran, D. S. Mehta, K. Agarwal, and B. S. Ahluwalia, "Multimodal on-chip nanoscopy and quantitative phase imaging reveals the nanoscale morphology of liver sinusoidal endothelial cells," Proc. Natl. Acad. Sci. **118**(47), e2115323118 (2021).
10. T. Dertinger, R. Colyer, G. Iyer, S. Weiss, and J. Enderlein, "Fast, background-free, 3D super-resolution optical fluctuation imaging (SOFI)," Proc. Natl. Acad. Sci. **106**(52), 22287–22292 (2009).
11. S. Culley, K. L. Tosheva, P. M. Pereira, and R. Henriques, "SRRF: Universal live-cell super-resolution microscopy," Int. J. Biochem. Cell Biol. **101**, 74–79 (2018).
12. O. Solomon, M. Mutzafi, M. Segev, and Y. C. Eldar, "Sparsity-based super-resolution microscopy from correlation information," Opt. Express **26**(14), 18238–18269 (2018).
13. I. Yahiatene, S. Hennig, M. Muller, and T. Huser, "Entropy-based super-resolution imaging (ESI): From disorder to fine detail," ACS Photonics **2**(8), 1049–1056 (2015).
14. K. Agarwal and R. Macháň, "Multiple signal classification algorithm for super-resolution fluorescence microscopy," Nat. Commun. **7**(1), 13752 (2016).
15. L.-H. Yeh, L. Tian, and L. Waller, "Structured illumination microscopy with unknown patterns and a statistical prior," Biomed. Opt. Express **8**(2), 695–711 (2017).
16. M. G. Gustafsson, "Surpassing the lateral resolution limit by a factor of two using structured illumination microscopy," J. Microsc. **198**(2), 82–87 (2000).
17. E. Mudry, K. Belkebir, J. Girard, J. Savatier, E. Le Moal, C. Nicoletti, M. Allain, and A. Sentenac, "Structured illumination microscopy using unknown speckle patterns," Nat. Photonics **6**(5), 312–315 (2012).
18. M. G. Gustafsson, "Nonlinear structured-illumination microscopy: wide-field fluorescence imaging with theoretically unlimited resolution," Proc. Natl. Acad. Sci. **102**(37), 13081–13086 (2005).
19. R. Heintzmann and T. Huser, "Super-resolution structured illumination microscopy," Chem. Rev. **117**(23), 13890–13908 (2017).
20. E. H. Rego, L. Shao, J. J. Macklin, L. Winoto, G. A. Johansson, N. Kamps-Hughes, M. W. Davidson, and M. G. Gustafsson, "Nonlinear structured-illumination microscopy with a photoswitchable protein reveals cellular structures at 50-nm resolution," Proc. Natl. Acad. Sci. **109**(3), E135–E143 (2012).
21. G. Ball, J. Demmerle, R. Kaufmann, I. Davis, I. M. Dobbie, and L. Schermelleh, "SIMcheck: a toolbox for successful super-resolution structured illumination microscopy," Sci. Rep. **5**(1), 15915 (2015).
22. K. Samanta, S. Sarkar, S. Acuna, J. Joseph, B. S. Ahluwalia, and K. Agarwal, "Blind super-resolution approach for exploiting illumination variety in optical-lattice illumination microscopy," ACS Photonics **8**(9), 2626–2634 (2021).

23. S. Acu na, I. S. Opstad, F. Godtliebsen, B. S. Ahluwalia, and K. Agarwal, "Soft thresholding schemes for multiple signal classification algorithm," Opt. Express **28**(23), 34434–34449 (2020).
24. I. S. Opstad, D. H. Hansen, S. Acu na, F. Ströhl, A. Priyadarshi, J.-C. Tinguely, F. T. Dullo, R. A. Dalmo, T. Seternes, B. S. Ahluwalia, and K. Agarwal, "Fluorescence fluctuation-based super-resolution microscopy using multimodal waveguided illumination," Opt. Express **29**(15), 23368–23380 (2021).
25. A. Descloux, K. S. Grußmayer, and A. Radenovic, "Parameter-free image resolution estimation based on decorrelation analysis," Nat. Methods **16**(9), 918–924 (2019).